

Article

Field-Oriented Driving/Braking Control for Electric Vehicles

Shang-Ming Liu ¹, Chia-Hung Tu ¹, Chun-Liang Lin ^{1,*}  and Van-Tsai Liu ²

¹ Department of Electrical Engineering, National Chung Hsing University, Taichung 407, Taiwan; kendirengrey@gmail.com (S.-M.L.); alex1983623@hotmail.com (C.-H.T.)

² Department of Electrical Engineering, National Formosa University, Yunlin 632, Taiwan; vtliu@nfu.edu.tw

* Correspondence: chunlin@dragon.nchu.edu.tw

Received: 16 August 2020; Accepted: 8 September 2020; Published: 10 September 2020



Abstract: Most electric vehicles use regenerative brakes, since this kind of braking system design recycles electromotive force to increase electric power endurance during braking. This research proposes a sensor-free, integrated driving and braking control system that uses a space-vector-pulse-width module to synthesize stator current by purpose. It calculates the rotor position angle of the motor by detecting variation in the stator current and completes a closed-loop control. When the motor receives a brake command, the controller changes the inverter-switching sequence to generate reverse torque and a magnetic field to complete the driving or braking function using field-oriented control (FOC). This provides a smoother and more accurate motor control than sinusoidal commands with Hall feedback. Compared to the regenerative brake and rheostatic brake, the proposed braking system has a powerful braking torque and shorter reaction time. Comparisons of reaction times for a modified four-wheel electric vehicle equipped with a permanent magnet synchronous motor under neutral-sliding-status, FOC based braking, and short-circuit braking were conducted.

Keywords: electric vehicle; motor; driver; brake; field-oriented control (FOC)

1. Introduction

Currently, most electric vehicles follow the design of regenerative braking, which converts lost energy back into the electric vehicle's battery via the inverter. There have been studies discussing regenerative braking with various approaches, such as [1,2]. Some research has adopted regenerative braking under extreme conditions, such as [3]. In [4], the authors combined three torque control methods in regenerative braking design. In [5], the authors propose a benchmark for studies related to regenerative braking; it appears that there is still room to improve. The paper of [6] presented an efficient to save energy under the circumstance of regenerative braking. While regenerative braking has been shown to be effective, there are unavoidable limitations of this kind of system, as depicted in [7,8]. One limitation is that the back electromotive force (EMF) is in general lower than the battery voltage level. Therefore, during braking, a voltage booster such as a transformer is needed. Another limitation is that when the battery is full and the recharge current continuously exceeds the battery's charging current limits, then energy resulting from the back-EMF must be dissipated to a resistor, which is a waste of energy.

Most published studies focused on the braking system design of motors adopt short-circuit braking [9,10], which directly converts the back-EMF to braking torque and apply the technology to electric bicycles and motorcycles [11–13]. Even though the braking effect is obvious, it may cause high-surge voltage and current under heavy loading. To revise the disadvantage of short-circuit braking, a reverse-field brake with rheostat, called a rheostatic brake, was proposed in [14], which can

be applied at any speed. However, it causes poor braking performance when the vehicle speed is decreasing—which leads to relatively low braking torque.

This research proposes an integrated driving and braking system for electric vehicles that adopts a senseless field-oriented control (FOC) method to achieve a compromise between braking performance and hardware reliability. Different from the traditional FOC algorithm [15,16] of braking systems, we propose an idea by reversing the direction of the magnetic field force of the permanent magnet (PM) synchronous motor (PMSM) stator coil from driving to braking—like the plug brake [17]. The plug brake has been commonly adopted in heavy systems and can stop a controlled object quickly during high-inertia rotating status. Technically, a plugging brake drives the electrical machine to the opposite direction. When receiving the braking signal, reverse rotor torque is synthesized by changing the direction of the current on the power transistors. We show that the same idea is applicable to the current design. The experimental results experiments shown here use this approach.

2. PMSM Model

There are two kinds of permanent magnet (PM) brushless motors: BLDCM [18], that have a trapezoidal-shaped back-EMF and PMSM, that have a sinusoidal one. For PMSM, there are two categories in terms of placement: surface-mounted PMSM (SPMSM) and interior PMSM (IPMSM). Although the specially skewed poles in a SPMSM are easily magnetized, they may fly apart from the rotor during high-speed operations as shown in Figure 1a. The IPMSM has an interior-mounted permanent magnet inside the rotor and has high performance under high-speed operation, as illustrated in Figure 1b.

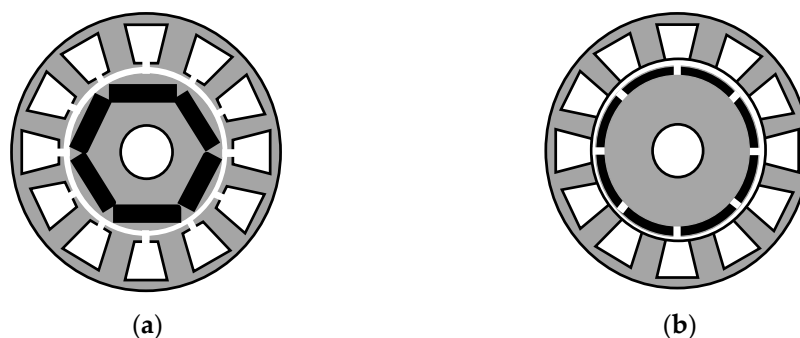


Figure 1. Structure of permanent magnet synchronous motor (PMSM). (a) Interior permanent magnet synchronous motor (IPMSM) and (b) surface-mounted permanent magnet synchronous motor (SPMSM).

We consider IPMSM as the experimental model in this research task, as by experience, BLDCM is not suitable for FOC. An equivalent circuit diagram of the PMSM is shown in Figure 2. We assume that the loss of vortex, magnetic hysteresis and damper winding are negligible and the air gap between the stator and the rotor is uniform.

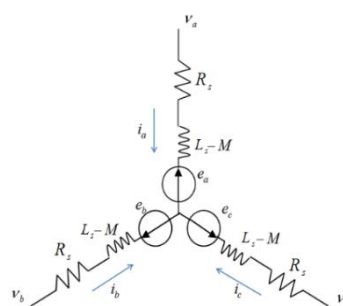


Figure 2. Equivalent circuit of the PMSM.

The three-phase motor circuit equation can be derived by the Kirchhoff circuit laws as:

$$\frac{d}{dt} \begin{bmatrix} i_a \\ i_b \\ i_c \end{bmatrix} = \frac{1}{L_s - M} I_3 \begin{bmatrix} V_{AQ} \\ V_{BQ} \\ V_{CQ} \end{bmatrix} - R_s I_3 \begin{bmatrix} i_a \\ i_b \\ i_c \end{bmatrix} - \begin{bmatrix} e_a \\ e_b \\ e_c \end{bmatrix} \quad (1)$$

where v_a, v_b, v_c are three phase voltages, respectively, i_a, i_b, i_c are three phase currents, respectively, R_s is motor internal resistor, I_3 is 3×3 identity matrix, L_s is self-inductance, M is mutual inductance and e_a, e_b, e_c are the three phase electromotive forces, respectively.

The demagnetization risk is considered for normal working conditions, and even for extreme cases such as motor running for a long period of time, or braking suddenly. The extreme conditions may cause an increase in temperature. If the motor is working below the knee-point in the BH-curve with the y -axis referred to the magnetic flux density and the x -axis referred to magnetic field strength [19], the permanent magnet will become demagnetized and cannot be recovered. Critical situations causing irreversible demagnetization are depicted in [20].

In addition, high temperature increases the risk of PMSM irreversible demagnetization by a right shift in the BH-curve, which clearly explains the relationship between temperature and demagnetization [19].

A three-phase short circuited will result in a lower working point until the motor stops, which generates a large external demagnetization field. The starting process of the motor also causes demagnetization. Influencing factors include loading, inertia and time costs. During the PMSM starting process, an external field is generated by the stator and rotor currents. When the relative angle of rotation between two magnetic fields is within $\pi/2$ and $3\pi/2$ degrees, a low working point is achieved, and the external field is in the demagnetization field. From the fact above, the duty cycle of the pulse-width modulation (PWM) for determining the braking command should be appropriately managed to avoid critical operations.

3. Control Strategy

3.1. System Architecture

FOC is one of the commonly known vector control methods for motors [15] that transform a three-phase time and speed-dependent system into a two-coordinate time invariant system. FOC uses torque and flux components as the input references d and q coordinates. The control unit first calculates the reference of the corresponding current component as determined by the drive's speed control. Then, a proportional-integral (PI) controller is applied to track the measured current components at their reference values.

The FOC flow chart is mainly composed of current detection, coordinate transformation, PI control algorithm and the space-vector pulse width module (SVPWM). First, the motor currents i_a and i_b are measured by current detection sensors. These two components are the input for the Clarke transformation. Then, the outputs i_α and i_β are generated by this module and fed to the Park transformation. The Park transformation results in the current in the d, q rotating reference frame. The outputs are designated as i_d and i_q , and the two components are compared with the flux references i_{dref} and the torque reference i_{qref} .

When a speed FOC is used, the torque command i_{qref} refers to the output of speed regulator. On the other hand, the rotor's position and speed are directly measured by a speed estimator. The rotational speed is used to generate the rotating coordinate axis of the rotor synchronization, and the AC-coordinate is converted into a DC-coordinate system. Then, the output current is sent to a PI controller and is converted into voltage signals V_q and V_d , outputs of the current regulators are V_{dref} and V_{qref} . The two outputs are applied to conduct an inverse Park transformation and generate another two outputs $V_{\alpha ref}$ and $V_{\beta ref}$. $V_{\alpha ref}$ and $V_{\beta ref}$ are components of the stator vector voltage in the

(α, β) coordinate system and fed to the space vector PWM. Finally, the outputs of the final block are the commands that drive the inverter. This completes the closed-loop control of the current.

3.2. Driver Design

The inverter topology is shown in Figure 3. Here, V_s denotes the voltage source with a capacitor C . There are six insulated gate bipolar transistors (IGBTs). It can be simplified to better understand how SVPWM works. Replacing the two-bridge leg-IGBTs by a switch that shows that either the top or the bottom IGBT is closed. It is possible to simplify from two IGBTs to a switch because only an IGBT in each bridge leg can be closed, and an IGBT must be closed in each leg to have a three phase current flowing. The simplified diagram is shown in Figure 4. There are six basic vectors representing different voltage sources applied to the connected port of the motor. The eight SVPWM states move from $V_0(000) \rightarrow V_1(001) \rightarrow V_2(011) \rightarrow V_3(010) \rightarrow V_4(110) \rightarrow V_5(100) \rightarrow V_6(101) \rightarrow V_7(111)$ with various voltage combination of 0, $-V_s$ and v_s imposed on V_{uv} , V_{vw} and V_{wu} .

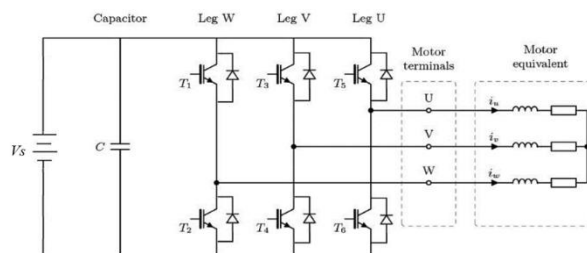


Figure 3. Simplified inverter topology.

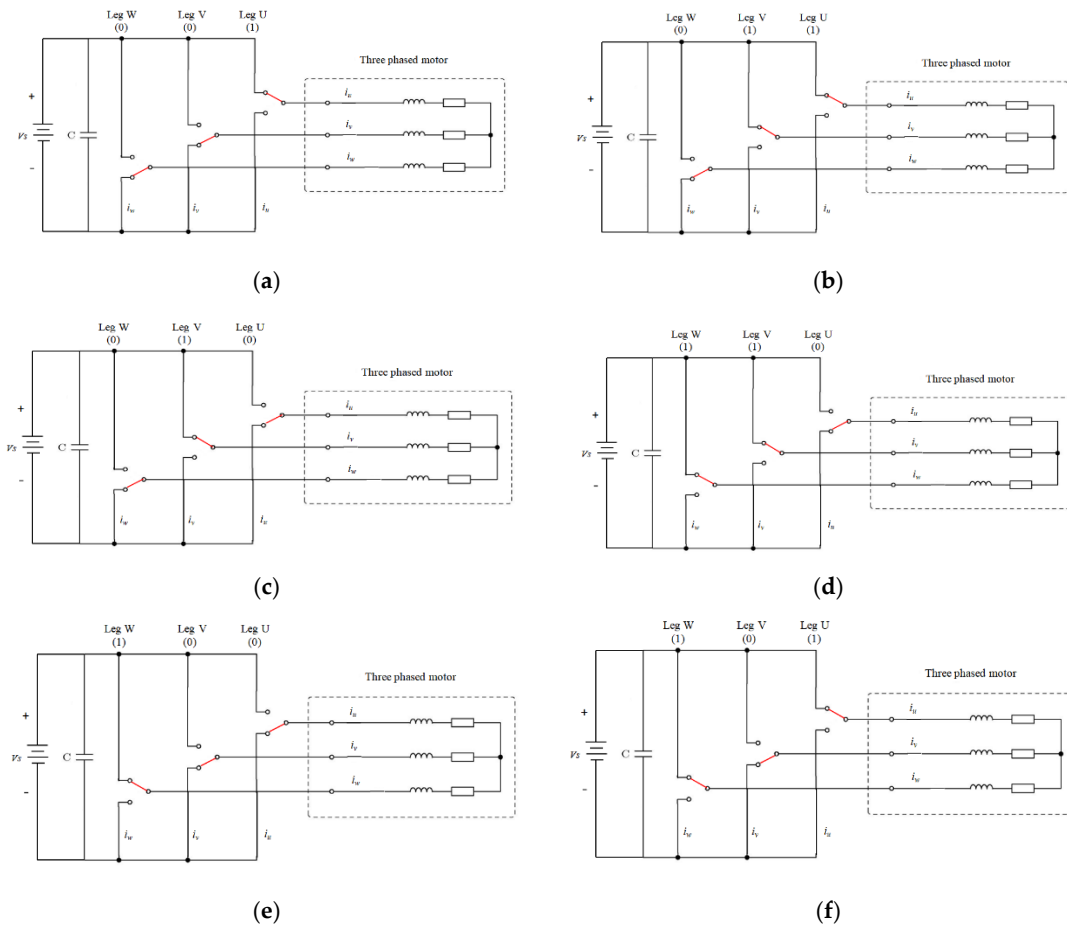


Figure 4. SVPWM of V_1 – V_6 . (a) SVPWM of V_1 (0,0,1); (b) SVPWM of V_2 (0,1,1); (c) SVPWM of V_3 (0,1,0); (d) SVPWM of V_4 (1,1,0); (e) SVPWM of V_5 (1,0,0); (f) SVPWM of V_6 (1,0,1).

The PMSM model in the rotor reference (d–q) frame is given by:

$$\frac{d}{dt}I_d = -\frac{R_s}{L_d}I_d + \omega_r \frac{L_q}{L_d}I_q + V_d \quad (2)$$

$$\frac{d}{dt}I_q = -\frac{R_s}{L_q}I_q - \omega_r \frac{L_d}{L_q}I_d - \frac{1}{L_q}\varphi_f\omega_r + V_q \quad (3)$$

where

$$\varphi_d = L_d I_d + \varphi_f, \quad \varphi_q = L_q I_q \quad (4)$$

in which L_q and L_d are, respectively, the d , q -axis inductances, I_d , I_q are, respectively, the d , q stator currents, P is the number of pole pair, φ_f is the mutual flux due to magnet, R_s is the stator resistor, V_d and V_q are the d , q -axis voltages and L_s is the self inductance.

The electromagnetic torque T_e is obtained as follows:

$$T_e = \frac{3}{2}P[(L_d - L_q)I_d I_q + I_q \varphi_f] \quad (5)$$

In this equation, if $I_d = 0$, the d -axis flux linkage φ_d is fixed. Since φ_f is constant for a PMSM, the electromagnetic driving torque T_m is determined by:

$$T_m = \frac{3}{2}P\varphi_f I_q \quad (6)$$

The current vector is produced in the FOC axis and the rotor flux is generated only in the q -axis. It is capable of achieving the maximal torque because the torque generated by the motor is proportionally linear to the q -axis current where the d -axis rotor flux remains as a constant. By this feature, one can use the electromagnetic torque not only in driving the motor, but to realize the function of motor brake to minimize the torque ripple of commutation.

3.3. Brake Control Design

Plug braking—also called as the counter-current braking—is a suitable electrical braking method for PMSM. It is obtained by changing the phase sequence of the input current that braking energy is dissipated within the motor. Plug braking differ greatly from rheostatic braking and regenerative braking, because plug braking requires energy to supply the braking force. On the contrary, the braking force is strong enough to be used in emergency situations, while the other two are not.

The principle of plug braking is to change the direction of rotating magnetic field by alternating the three-phase current's phase sequence. The PMSM model was used for high-performance control and characterized in the Section 2. It was derived in different reference frames, such as the d–q frame for the control purposes.

For the braking system design, we realize the plug braking by reversing the eight SVPWM switching states to the motor driver design to go from $V_7(111) \rightarrow V_6(101) \rightarrow V_5(100) \rightarrow V_4(110) \rightarrow V_3(010) \rightarrow V_2(011) \rightarrow V_1(001) \rightarrow V_0(000)$ with voltage combination of 0, $-V_s$ and V_s given to V_{uv} , V_{vw} and V_{wu} . This makes it feasible to control the motor rotation by fixing the reference frame to a particular motor quantity.

Traditional regenerative brakes can be easily realized here for the purpose of recharging the battery. This can be fulfilled by disconnecting the connection between driving unit and inverter and directing the back-EMF via the inverter to the battery as shown in Figure 4, but with inverse SVPWM switching states. It should be noted that since the IGBT does not have body diode, therefore, a diode must be added to the collector and the emitter for rectifying the sinusoidal stator waveform.

Next, to follow the preceding design [10], the function of electromagnetic braking system is also built to keep the vehicle slip ratio staying within an ideal range for safety brake, i.e., ABS, by adjusting duty cycle of the driving current flow.

Figure 5 illustrates the braking control scheme where M is vehicle weight, T_m is driving torque, J_w is inertia of the driving wheel, ω_w is angular speed of the driving wheel, T_B is braking torque, B_w is damping coefficient of the driving wheel, r is radius of the driving wheel, and $\hat{\lambda}$ is the estimated value of the vehicle slip ratio λ defined by:

$$\lambda = \frac{V_w - V}{\max(V_w, V)} \tag{7}$$

where $V_w = \omega_w r$ denotes the tangential speed of the motor driving wheel and V is the vehicle speed. The estimated slip ratio can be obtained via:

$$\dot{\hat{\lambda}} = \left[\frac{\dot{\omega}_w}{\omega_w} - \frac{F}{rM\omega_w} (1 + \hat{\lambda}) \right] (1 + \hat{\lambda}) \tag{8}$$

where F is friction force, if $\dot{V}_w < \dot{V}(2 + \lambda + \hat{\lambda})$. Since $\lambda \ll 1$ and $\dot{V}_w \leq \dot{V} \leq 0$ during vehicle braking, the sufficient condition holds in most practical road driving.

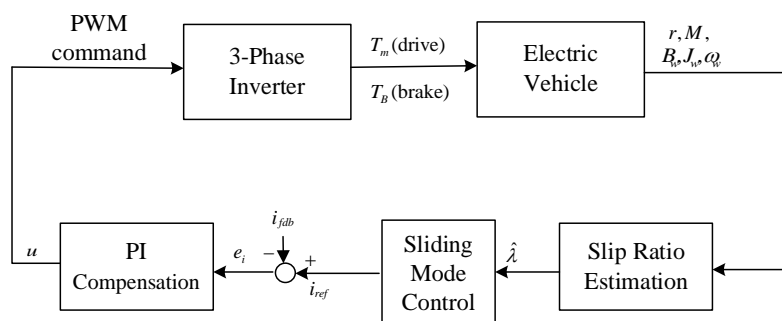


Figure 5. Architecture of the braking control system.

Sliding-mode control (SMC) for regulation of the slip ratio is adopted to ensure the best tire-to-road adhesion. This is used to avoid wheel brake-lock during emergency braking. The ideal value of the slip ratio λ_{ideal} lies in the range of 0.2–0.3 for general dry road surfaces. The slip-ratio control is developed to suppress the slip-ratio error $\Delta\lambda = \hat{\lambda} - \lambda_{ideal}$ by the SMC. Moreover, PI compensation is included to track the reference current computed by the SMC. The PI controller is given by $u = (K_p + \frac{1}{s}K_i)e_i$ where K_p and K_i are, respectively, the proportional and integral control gains and $e_i = i_{ref} - i_{fdb}$ with i_{ref} as the reference input generated by the SMC and i_{fdb} being the feedback braking current measured via a current sensor from the motor. One is referred to [10] for details of the theoretical development.

4. Implementation

4.1. Hardware Design

As shown in Figure 6, an electric vehicle was modified from a 1500-cc gasoline-powered sedan with 25-series lead–acid batteries assembled as the power tank. The details of the connection of the group of batteries is shown in Figure 7. Each battery was fully charged at 12.6 volts, the bus voltage was boosted to exceed 300 volts with four no-fuse breakers installed to protect the power system. The implementation of the battery recharging system is another issue which will come in another publication.



Figure 6. Electric vehicle modified from a gas-powered sedan for experimental tests.



Figure 7. Twenty-five lead acid batteries assembled as the high-voltage power source.

The hardware architecture is shown in Figure 8. The system consisted of three parts: the digital signal controller (DSC), the inverter and the PMSM.

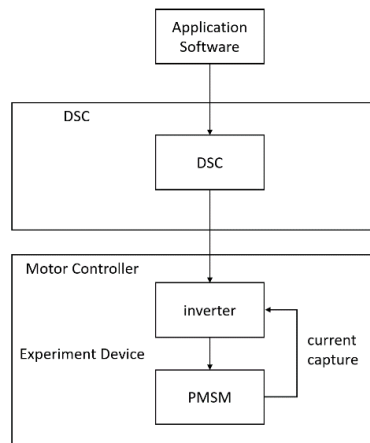


Figure 8. Hardware architecture.

The sensorless FOC system requires a high-speed communication path to ferry a significant amount of data back and forth. We adopted the microchip MCLV-2 to build the motor driver.

The inverter circuit is displayed in Figure 9. The purpose of inverter is to change the input DC voltage to a three-phase AC voltage by adjusting the magnitude and frequency. We use the 300-volt series batteries as the input voltage source and six IGBTs of BSM150G60DLC. The efficiency of the IGBTs used in high voltage and high-power applications is much higher than MOSFETs for motor driving. We used the SVPWM to modulate the stator current by the inverter consisting of six IGBTs and an added on-off timing “delay” (dead time) to prevent from short circuits at the same leg.



Figure 9. Integrated driving/braking inverter.

Figure 10 shows the PMSM used in the experiment with specifications listed in Table 1.



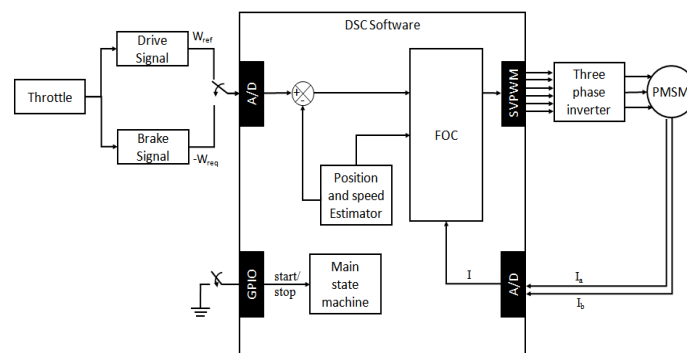
Figure 10. PMSM used in the experimental electric vehicle.

Table 1. PMSM specifications.

Model	LDSM230-D
Number of poles	8
Power (kw)	15
Torque (Nm)	90.1
NR (RPM)	1500
Max current (A)	55.5
Ke (V)	92.4
Back-eEMF type	Sine wave

4.2. Software Design

This research task proposes a compound design to integrate the motor-braking unit with the driver unit in the sensorless FOC scheme. The system architecture is shown in Figure 11. When the motor starts, the difference between the measured speed (W_{req}) and the reference speed (W_{ref}) is calculated and processed via the PI controller. Whenever the motor receives a braking command, W_{ref} is replaced by $-W_{ref}$ and the motor decelerates according to the braking control command calculated by the algorithm depicted in Section 3.3 to realize the braking procedure.

**Figure 11.** System architecture.

The control algorithm realized in the MCLV-2 was prepared in C language while DSP subroutines were realized in assembly language.

5. Representative Results

There are several methods which can be used to stop a running motor as depicted. First, we test the motor on a no-load basis. Figures 12–14 show the motor stopping running with a neutral sliding status, a short-circuit brake, and the FOC reverse brake at 450 rpm and 950 rpm, respectively.

The modified FOC reverse-braking method was compared with other approaches as shown in Table 2. When the PMSM was running at 950 rpm using short-circuit braking, the peak current was up to 75.2 A. Results were averaged after conducting 10 experimental runs. It will be extremely unacceptable if the rated current of the PMSM is only 55.5 A. Therefore, it is not appropriate to use short-circuit braking for high-power motors because it risks damage to the driving circuit. For the two approaches, the FOC reverse-braking showed better performance on average.

Table 2. Comparison of various braking methods.

Braking Condition (rpm)	Braking Type	Peak Current (A)	Peak Voltage (V)
450	Neutral sliding	3.4	300
450	Short-circuit braking	42	304
450	FOC reverse-braking	9.4	304
950	Neutral sliding	4.8	300
950	Short-circuit braking	75.2	304
950	FOC reverse-braking	28	404

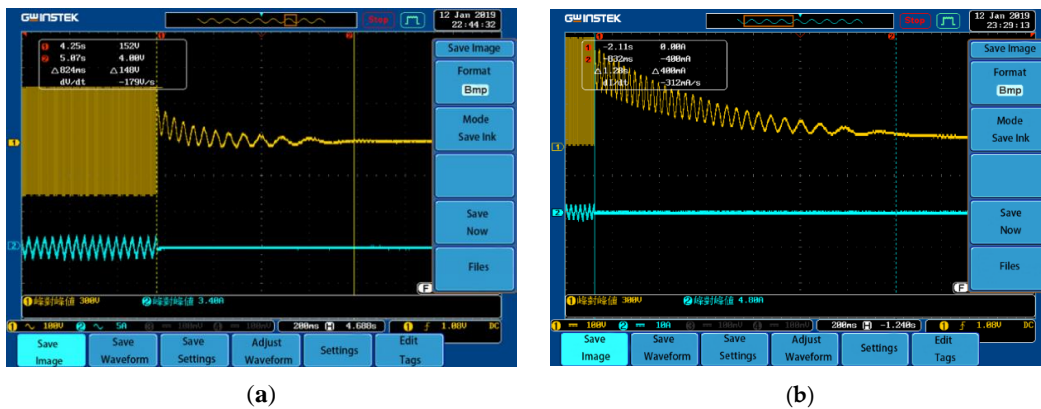


Figure 12. PMSM working under sliding conditions. (a) 450 rpm; (b) 950 rpm.

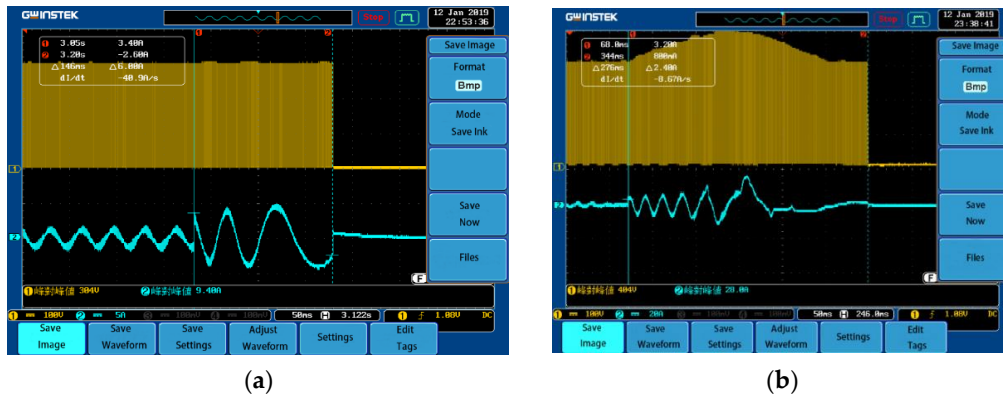


Figure 13. PMSM working under the FOC reverse-braking mode. (a) 450 rpm; (b) 950 rpm.

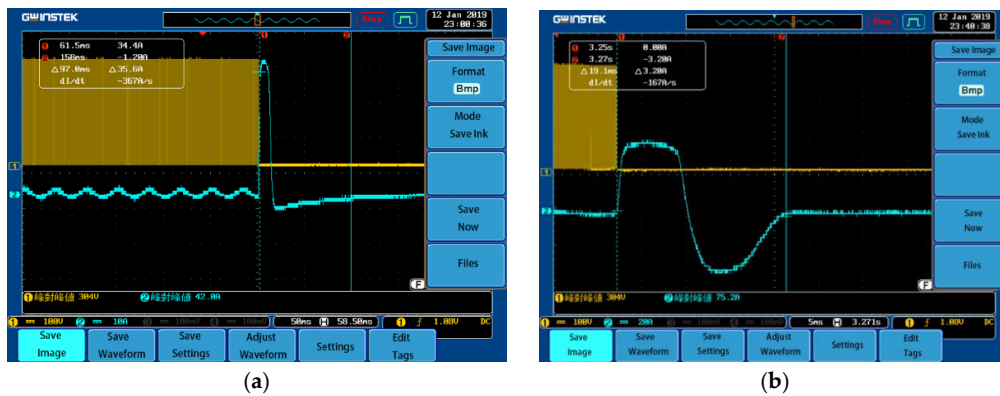


Figure 14. PMSM working under short-circuit braking mode. (a) 450 rpm; (b) 950 rpm.

For an on-road video demonstration of the experimental tests please see [21–26]. In this, functional tests of motor driving and braking for the modified electric vehicle shown in Figure 6 on various road conditions are presented.

6. Conclusions

Most previous studies reversed the magnetic field of a motor by changing the switching sequence of power transistors to obtain a powerful value of reverse torque with a rheostatic brake. However, it always performs poorly at low speed due to the small and quickly decreasing back-EMF and induction of significant motor vibration while using six-step commutation. We present here a framework to facilitate efficient braking performance during low vehicle speeds by using a sensorless FOC-based driving-braking control scheme for electric vehicles. The FOC system exhibits smaller ripple, less noise and good efficiency as compared with traditional six-step commutation. Moreover, the FOC reverse-braking scheme exhibits acceptable response at both at high and low speeds. This advantage leads to better controllability during vehicle driving. Extensive on-road experiments conducted using an electric sedan verify the proposed approach.

7. Patents

C.L. Lin, E.P. Chen and Y.C. Chen, “Sensorless electronic brake control system,” Taiwan Patent No. I 664804, 2019.

C.L. Lin, C.Y. Chang and D.H. Chen, “Electric vehicle driving system for suppressing and distributing surge voltage and current caused by the back electromotive force during braking,” Taiwan Patent No. I 694015, 2020.

Author Contributions: Conceptualization, C.-L.L.; methodology, C.-L.L.; software, S.-M.L.; validation, S.-M.L. and C.-H.T.; formal analysis, S.-M.L. and C.-H.T.; investigation, S.-M.L. and C.-H.T.; resources, C.-L.L. and V.-T.L.; writing—original draft preparation, S.-M.L.; writing—review and editing, S.-M.L. and C.-H.T.; visualization, S.-M.L. and C.-H.T.; supervision, C.-L.L. and V.-T.L.; project administration, C.-L.L. and V.-T.L.; funding acquisition, C.-L.L. All authors have read and agreed to the published version of the manuscript.

Funding: This research was supported by the Ministry of Science and Technology, Taiwan under the grant MOST 106-2221-E-005-001-MY2.

Conflicts of Interest: The authors declare no conflict of interest.

References

1. Tzortzis, G.; Amargianos, A.; Piperidis, S.; Koutroulis, E.; Tsourveloudis, N.C. Development of a compact regenerative braking system for electric vehicles. In Proceedings of the Mediterranean Conference on Control and Automation, Torremolinos, Spain, 16–19 June 2015; pp. 102–108.
2. Luo, N.; Jiang, J.; Yu, A. Research on the control strategy of the regenerative braking system. In Proceedings of the International Conference on Mechatronics and Control, Harbin, China, 3–5 July 2014; pp. 2514–2517.
3. Itani, K.; Bernardinis, A.D.; Khatir, Z.; Jammal, A.; Oueidat, M. Regenerative braking modeling, control, and simulation of a hybrid energy storage system for an electric vehicle in extreme conditions. *IEEE Trans. Transp. Electrification*. **2016**, *2*, 465–479. [[CrossRef](#)]
4. Itani, K.; de Bernardinis, A.; Khatir, Z.; Jammal, A. Optimal traction and regenerative braking reference current synthesis for an IPMSM motor using three combined torque control methods for an electric vehicle. In Proceedings of the IEEE Transportation Electrification Conference & Expo, Dearborn, MI, USA, 27–29 June 2016; pp. 1–6.
5. Fajri, P.; Lee, S.; Prabhala, V.A.K.; Ferdowsi, M. Modeling and integration of electric vehicle regenerative and friction braking for motor/dynamometer test bench emulation. *IEEE Trans. Veh. Technol.* **2016**, *65*, 4264–4273. [[CrossRef](#)]
6. Zhang, X.; Gohlich, D.; Li, J. Energy-efficient torque allocation design of traction and regenerative braking for distributed drive electric vehicles. *IEEE Trans. Veh. Technol.* **2018**, *67*, 285–295. [[CrossRef](#)]

7. Pengyu, W.; Qingnian, W.; Wangwei; Naiwei, Z. The affect of motor efficiency on regenerative braking at low-speed stage. In Proceedings of the International Conference on Energy and Environment Technology, Guilin, China, 16–18 October 2009; pp. 388–391.
8. Gokce, C.; Ustun, O.; Yeksan, A.Y. Dynamics and limits of electrical braking. In Proceedings of the International Conference on Electrical and Electronics Engineering, Bursa, Turkey, 28–30 November 2013; pp. 268–272.
9. Cody, J.; Göl, Ö.; Nedic, Z.; Nafalski, A.; Mohtar, A. Regenerative braking in an electric vehicle. *Zesz. Probl. –Masz. Elektr.* **2009**, *81*, 113–118.
10. Lin, C.L.; Yang, M.Y.; Chen, E.P.; Chen, Y.C.; Yu, Y.C. Novel antilock braking control system for electric vehicles. *IET J. Eng.* **2018**, *2018*, 60–67.
11. Lin, W.C.; Lin, C.L.; Hsu, P.M.; Wu, M.T. Realization of Anti-Lock braking strategy for electric scooters. *IEEE Trans. Ind. Electron.* **2014**, *61*, 2826–2833. [[CrossRef](#)]
12. Lin, C.L.; Tu, C.H.; Liu, M.K. Method of Adjus Electro-Magnetic Braking Force for Electric Bikes. Taiwan Patent No. I626190, 11 June 2018.
13. Lin, C.L.; Hsieh, M.C.; Chen, T.H. Integrated driving and braking control unit for electric bikes. *SAE Int. J. Veh. Dyn. Stab. NVH* **2018**, *2*, 223–242. [[CrossRef](#)]
14. Chen, Y.C.; Tu, C.H.; Lin, C.L. Integrated electromagnetic braking/driving control for electric vehicle using fuzzy inference. *IET Electr. Power Appl.* **2019**, *13*, 1014–1021. [[CrossRef](#)]
15. Zambada, J.; Deb, D. *Sensorless Field Oriented Control of a PMSM*; AN1078 of Microchip Technology Inc.: Chandler, AZ, USA, 2010; pp. 1–28.
16. Genduso, F.; Miceli, R.; Rando, C.; Galluzzo, G.R. Back EMF sensorless-control algorithm for high-dynamic performance PMSM. *IEEE Trans. Ind. Electron.* **2010**, *57*, 2092–2100. [[CrossRef](#)]
17. Jiang, J.; Holtz, J. An efficient braking method for controlled ac drives with a diode rectifier front end. *IEEE Trans. Ind. Appl.* **2001**, *37*, 1299–1305. [[CrossRef](#)]
18. Enrique, L. Carrillo Arroyo, Modeling and Simulation of Permanent Magnet Synchronous Motor Drive System. Master’s Thesis, University of Puerto Rico, San Juan, Puerto Rico, 2006.
19. Ruohu, S. *Demagnetization of Permanent Magnets in Electrical Machines*; Doctoral School of Energy-and Geo-Technology: Kuressaare, Saaremaa, Estonia, 2007; pp. 181–185.
20. Fu, W.N.; Ho, S.L. Dynamic demagnetization computation of permanent magnet motors using finite element method with normal magnetization curves. *IEEE Trans. Appl. Supercond.* **2010**, *20*, 851–855. [[CrossRef](#)]
21. Liu, S.M.; Tu, C.H.; Lin, C.L.; Liu, V.T. Video demonstration: Test of Driving at the NCHU Campus (24°07′26.7″ N 120°40′30.2″ E/24.124083° N 120.675056° E). Available online: <https://youtu.be/LWUFJMBLu8s> (accessed on 3 September 2020).
22. Liu, S.M.; Tu, C.H.; Lin, C.L.; Liu, V.T. Video demonstration: Test of Brake on the Plane. Available online: https://youtu.be/1QbzRgUlt_Q (accessed on 3 September 2020).
23. Liu, S.M.; Tu, C.H.; Lin, C.L.; Liu, V.T. Video demonstration: Test of Engine Brake (Generated by the Motor) on the Down Ramp Lane-Front View. Available online: <https://youtu.be/quXreRd1Ofc> (accessed on 3 September 2020).
24. Liu, S.M.; Tu, C.H.; Lin, C.L.; Liu, V.T. Video demonstration: Test of Engine Brake (Generated by the Motor) on the Down Ramp Lane-Rear View. Available online: <https://youtu.be/X0m6POyrdO4> (accessed on 3 September 2020).
25. Liu, S.M.; Tu, C.H.; Lin, C.L.; Liu, V.T. Video demonstration: Test of Driving on the Climbing Lane-Front View. Available online: <https://youtu.be/rmoI10k55cs> (accessed on 3 September 2020).
26. Liu, S.M.; Tu, C.H.; Lin, C.L.; Liu, V.T. Video demonstration: Test of Driving on the Climbing Lane-Rear View. Available online: <https://youtu.be/zpTgKn-jnww> (accessed on 3 September 2020).

